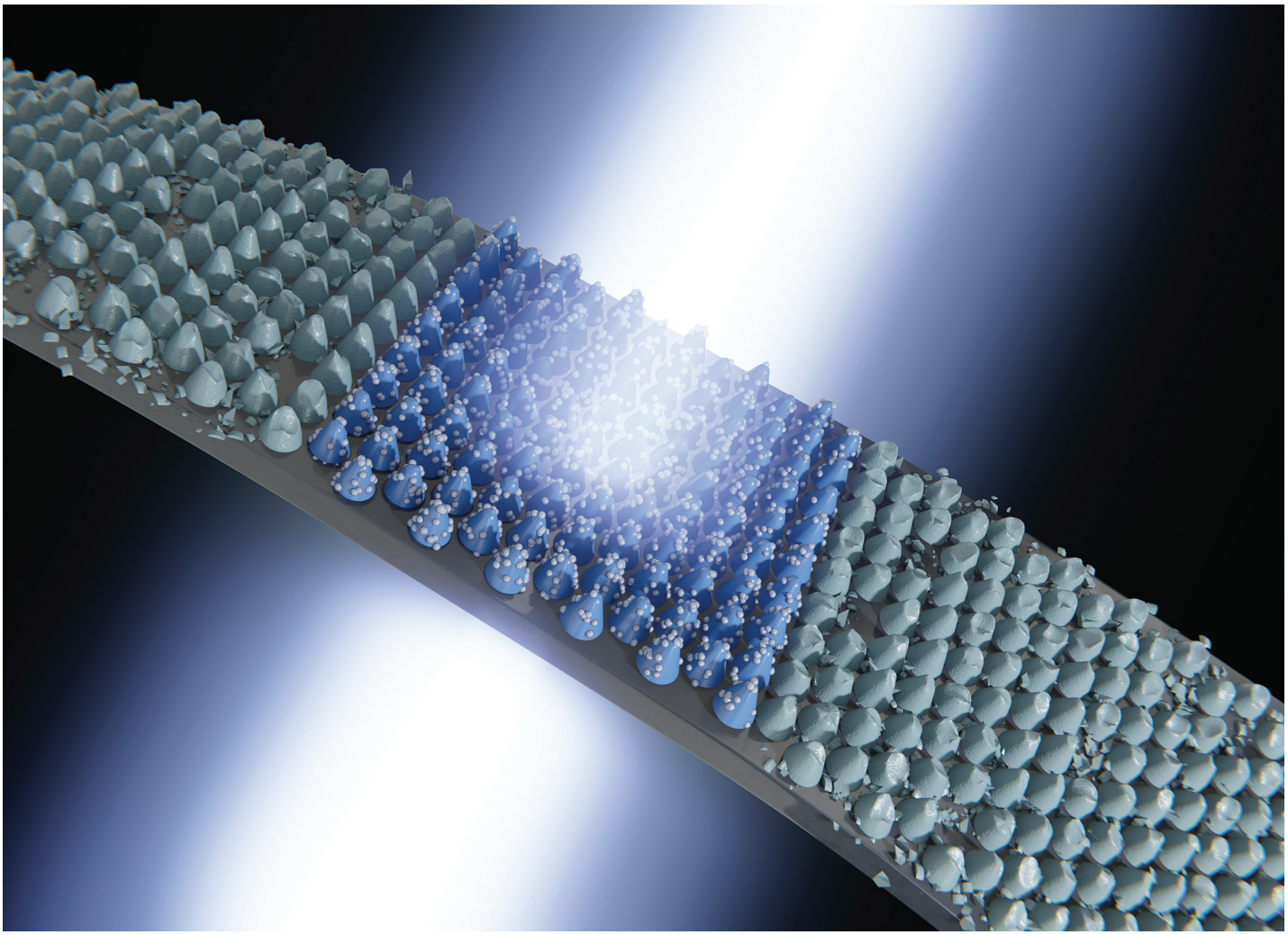

Showcasing research from IMDEA Nanoscience, Madrid, Spain.

Single-imprint moth-eye anti-reflective and self-cleaning film with enhanced resistance

This work presents nanoimprinted moth-eye surface nanocomposite films exhibiting multifunctional broadband anti-reflective and photo-induced self-cleaning properties with improved mechanical resistance. The anti-reflective films are produced in combined processing steps of titanium dioxide nanoparticle coating and surface imprinting of moth-eye nanostructures. Nanoparticle - polymer blending and formation of reinforced sub-wavelength surface nanocomposite features is achieved simultaneously.
This methodology represents a practical approach for producing nanoimprinted surfaces with superior mechanical properties and multi functionality. The films are suitable for flexible and portable solar devices.

As featured in:

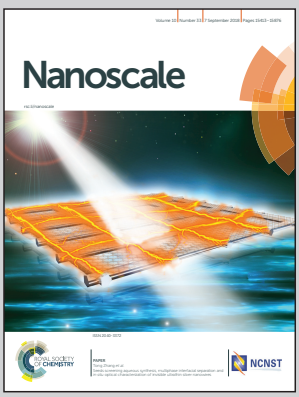

See Isabel Rodríguez *et al.*, *Nanoscale*, 2018, **10**, 15496.

ROYAL SOCIETY OF CHEMISTRY

rsc.li/nanoscale

Registered charity number: 207890

Nanoscale

PAPER

View Article Online
View Journal | View Issue

Cite this: *Nanoscale*, 2018, **10**, 15496

Single-imprint moth-eye anti-reflective and self-cleaning film with enhanced resistance†

Iván Navarro-Baena, [a] Alejandra Jacobo-Martín, [a] Jaime J. Hernández, [a] Jose R. Castro Smirnov, [a] Felipe Viela, [a] Miguel A. Monclús, [b] Manuel R. Osorio, [a] Jon M. Molina-Aldareguia [b] and Isabel Rodríguez *[a]

Antireflective transparent materials are essential for a myriad of applications to allow for clear vision and efficient light transmission. Despite the advances, efficient and low cost solutions to clean antireflective surfaces have remained elusive. Here, we present a practical approach that enables the production of antireflective polymer surfaces based on moth-eye inspired features incorporating photoinduced self-cleaning properties and enhanced mechanical resistance. The methodology involves the fabrication of sub-wavelength moth-eye nanofeatures onto transparent surface composite films in a combined processing step of nanoparticle coating and surface nanoimprinting. The resulting surfaces reduced the optical reflection losses from values of 9% of typical PMMA plastic films to an optimum value of 0.6% in the case of double-sided moth-eye nanoimprinted films. The composite moth-eye topography also showed an improved stiffness and scratch resistance. This technology represents a significant advancement not limited by scale, for the development of antireflective films for low cost application products.

Received 22nd March 2018,
Accepted 2nd May 2018

DOI: 10.1039/c8nr02386g

rsc.li/nanoscale

1. Introduction

A large number of products require strategies to avoid undesirable reflections and glare for example electronic displays, optics and lighting, solar panels, architectural glazing, storefronts, *etc*. A low cost solution employed today is the application of antiglare coatings to eliminate external reflections. These coatings make use of diffuse scattering to disperse the reflected light. Diffusion works by reducing the coherence of the image that is reflected, making it appear unfocused and as a trade-off, resolution and clarity are reduced.

Anti-reflective (AR) coatings represent a much more efficient approach.[1] The current AR coating strategies are based on the multilayer interference and quarter-wave principles.[2] Multilayer interference coatings are produced by interlayering non-absorbing, high and low refractive index materials. While this strategy is very effective and well established, it is costly and it is not suitable for low value added products. Quarter-wave coatings consist of a single quarter-wave layer of transparent material whose refractive index is the square root of the substrate's refractive index. Quarter-wave coatings are optimized for one single wavelength and one angle of incidence; hence, they have a very intense reflection colour and lack broadband antireflective properties.

An additional approach to realize AR optical properties is by creating a graded refractive index interface by means of surface texturization at subwavelength dimensions. These surfaces are also called moth-eye AR surfaces from where they were initially inspired.[3,4] Moth-eye AR surfaces impart antireflective properties to an interface not only over a broad spectral range but also over wide angles of incidence.[5,6] An additional important advantage is that they are very low cost potentially as they do not require additional materials or processing steps for production. High aspect ratio moth-eye like structures can sometimes display self-cleaning behaviour derived from superhydrophobicity by minimizing the adhesion of dirt particulates or easing their removal.[7]

Continuous nanoimprint processing is possibly the technology most suitable to produce moth-eye AR surfaces at the industrial scale for low value added products such as architectural windows or solar collectors where high volumes and large areas are required. In these products, not only reflection reduction is required, but additional functions, such as transparency, self-cleaning abilities, mechanical strength and durability will be of clear advantage. The fabrication of effective moth-eye AR polymer films by nanoimprinting has been

[a]*Madrid Institute for Advanced Studies in Nanoscience (IMDEA Nanoscience), C/Faraday 9, Ciudad Universitaria de Cantoblanco. 28049 Madrid, Spain. E-mail: i.rodriguez@imdea.org*
[b]*Madrid Institute for Advanced Studies in Materials (IMDEA Materials), C/Eric Kandel, 2, Tecnogetafe, Getafe. 28906 Madrid, Spain*
†Electronic supplementary information (ESI) available. See DOI: 10.1039/c8nr02386g

reported before[8–13] by large scale[14] and roll to roll[15] processes. However, for the practical implementation of the technology there are still several issues to resolve. Firstly, it is the fragility of the sub-wavelength cone-like features needed to produce moth-eye AR surfaces. In addition, the high transmittance of AR surfaces can be drastically reduced by the adsorption of contaminants from the atmosphere and or deterioration over time primarily due to photodegradation and wear in exterior environments.[16,17]

Titanium dioxide (TiO_2), also known as titania, remains as one of the most widely used additives for its chemical stability and properties derived from its semiconductor nature. Currently, titania micro or nanoparticles are added to paints, plasters or fabrics to impart properties such as UV-blocking, mechanical resistance, antimicrobial or self-cleaning properties.[18–21] In organic coatings or paint formulations, TiO_2 is employed for its dual function as a photocatalyst and as a photoabsorber.[22] As a photoabsorber, TiO_2 is an effective UV radiation screener of wavelengths from 280 nm to 400 nm and consequently it helps to inhibit polymer photodegradation and embrittlement due to polymer chain scission.[23]

As a photocatalyst, with a band gap of 3.2 eV, TiO_2 (anatase) absorbs photons with a wavelength of 388 nm and in the presence of water and oxygen, highly reactive radicals such as hydroxyl and hydroperoxyl radicals and activated oxygen species are produced which are capable of causing oxidative degradation of organic matter including contaminants.[24] These species may also give rise to photocatalytically induced hydrophilicity that is, the conversion of hydrophobic surface character to a hydrophilic one upon exposure to UV light.[25] TiO_2 supported nanoparticles have also found important applications in heterogeneous photocatalytic decontamination.[26–28] To prevent photocatalytic oxidative degradation in the case of organic host matrices, several strategies have been developed. Traditionally this has been avoided by using an inert interlayer to insulate the photooxidation activity often using a silica[29] or a polysiloxane layer.[30] More recently, TiO_2 functionalization with silane coupling agents[31] or hybrid sol–gel silane coatings[32] have emerged as more practical approaches for the preparation of photocatalytic coatings with reduced impact on the organic matrices. A more straightforward strategy employed in outdoor coating formulations is to use a low particle loading (*i.e.* $\leq$2%) where a compromise between achieving a sufficient photo-oxidation and UV shielding efficiency for a weathering resistance during the particular service life can be achieved.[33]

There have been a number of reports where graded refractive index surfaces have been conferred with self-cleaning ability primarily derived from TiO_2 photooxidation reactions together with an enhancement of surface wettability. In this line of work, Guldin *et al.* developed anti-reflective coatings based on a highly porous silica based network produced by silica sol gel chemistry incorporating TiO_2 nanocrystals.[34] The process required the steps of coating, annealing and plasma etching of the organic components, which makes processing complicated and difficult to implement in practice, particularly on flexible substrates. Moreover, porous AR thin films may be prone to water absorption, which will give rise to variations in the RI and degradation of transmittance. Nakata *et al.* coated TiO_2 nanoparticles onto a commercial PET prepatterned with moth-eye structures. A strong self-cleaning effect was achieved based on the hydrophilicity imparted by TiO_2 after UV irradiation. However, due to the thick layer of nanoparticles employed, a marked decrease in the film transparency was observed.[35] Kang *et al.* developed a nanoimprinted TiO_2 moth-eye layer on perovskite solar cells, reporting an improvement in the light harvesting efficiency. However, due to the high refractive indices of both TiO_2 layer and perovskites, the reflection reduction was only moderate.[36] TiO_2 has also been recently incorporated into a moth-eye inspired topography made of PDMS to act as a UV filter while preserving transparency.[37]

Due to the high elastic modulus of titania nanoparticles, the incorporation of the nanoparticles has in addition a reinforcement effect on polymer matrices.[38] However, a low load and adequate dispersion of nanoparticles within the polymer matrix is necessary to preserve transparency in optical films.

Here, we describe a first of its kind approach targeted to improve the current limitations of polymer based moth-eye AR surfaces. The methodology involves the fabrication in a single processing step of AR flexible polymer transparent films by nanoimprinting sub-wavelength moth-eye features onto a polymer surface loaded with TiO_2 nanoparticles. The surface acquires multiple properties including photoinduced self-cleaning and enhanced mechanical resistance while improving the optical transparency compared to the neat flat films. This methodology could be readily adapted *via* roll-to-roll to large area processing for applications such as architectural windows or flexible solar devices.

2. Experimental

2.1 Synthesis of TiO_2 nanoparticles

TiO_2 nanoparticles were prepared following the hydrothermal synthesis method described by Grätzel.[39] For this, 20 ml of titanium isopropoxide(IV) (Acros Organics) was added to 36 ml of deionised water and the mixture was stirred for one hour. The resulting product was filtered and washed three times with deionised water. The filtered product was placed into a Teflon-lined titanium autoclave and mixed with 3.9 ml of 0.6 M tetramethylammonium hydroxide (Sigma Aldrich). The reaction was carried out for 14 hours at 120 °C. Finally, the resulting colloid was centrifuged two times at 10 000 rpm for 10 min to remove aggregates. The final colloidal aqueous solution contained a concentration of nanoparticles of approximately 24 wt% with a mean diameter of 24 nm as measured by dynamic light scattering (Malvern Zetasizer). Wide angle X-ray diffraction (WAXD) measurements were performed at the BM26 beamline of the European Synchrotron Radiation Facility (ESRF, Grenoble) to confirm the formation of the

anatase phase of TiO_2. The detailed characterization of the nanoparticles is included in Fig. S1.†

2.2 Preparation of TiO_2–polymer substrates

Initially, a poly(methyl methacrylate) (PMMA) (Sigma Aldrich) solution in toluene (7.5 wt%) was spin-coated (1000 rpm) onto a PET (Hifi Industrial Film, 125 μm thickness) film disk of 5 cm diameter employed as a carrier. A PMMA layer of about 660 nm was obtained (see Fig. S2†). Next, the aqueous dispersion of TiO_2 nanoparticles was diluted with methanol at three different concentrations (0.1, 0.5 and 1 wt%) and these dispersions were spin-coated (3000 rpm) onto the previously layered PMMA film generating a TiO_2 nanoparticle film for the 0.5 and 1 wt% dispersions and a discontinuous particle layer for the case of 0.1 wt% dispersion (see Fig. S3†).

2.3 Nano-imprinting of the moth-eye AR TiO_2 composite films

The AR structures were created by a thermal nanoimprint process. Initially, a working mould of polydimethylsiloxane (PDMS) with the AR moth-eye topography was prepared from a master nickel anti-reflective mould (HT-AR-02, Temicon). This was achieved using two layers of PDMS: hard-PDMS (h-PDMS) (Gelest) and soft PDMS (Sylgard 184, Dow Corning). The h-PDMS was first mixed and cast onto the master nickel mould. After a period of 30 min for the filling the cavities, the mould was spin-coated (1000 rpm for 1 min) in order to obtain a homogeneous thin layer of h-PDMS. Subsequently, the h-PDMS was partially cured in an oven for 10 min at 80 °C. Then the PDMS precursor and initiator mixture were cast on the partially cured h-PDMS and placed in an oven at 80 °C for 24 hours to cure completely. Finally, the replicated working mould was peeled off and kept in a clean room environment.

Using the PDMS working mould, the prepared TiO_2–PMMA surfaces were imprinted at 170 °C at 45 bar of pressure for 5 min (Eitre 3 Nanoimprint Lithography System, Obducat). The different samples prepared were labelled as P-XT-AR, where "X" refers to the concentration of the TiO_2 dispersion employed.

2.4 Property characterization of AR TiO_2 composite films

The topography of the imprinted substrates was characterized by scanning electron microscopy (SEM) (Auriga FIB-SEM system, Zeiss) and atomic force microscopy (AFM) in tapping mode (Multimode 8 AFM with a Nanoscope V controller, Bruker).

The specular transmission and total reflection measurements were obtained using a Lambda 650 UV-Vis spectrophotometer (PerkinElmer) fitted with a 150 mm integrating sphere.

The photo-catalytic capacity of the AR composite films was measured through degradation assays of Rhodamine B (RhB) aqueous solution (5 mg L^{-1}). For this, the AR films were placed on a Petri dish with 12 ml of RhB solution. The substrates were first stored in darkness for 120 min to reach an adsorption–desorption equilibrium of RhB. Subsequently, the substrates were irradiated with UV light (UVASPOT 400/T, Honle) providing 80 mW cm^{-2} of light intensity for periods of 10 min while kept in an ice bath to avoid evaporation caused by heating. At these intervals, an aliquot was measured with a spectrophotometer at the peak of maximum absorbance (554 nm). The results of 4 different experiments were averaged for each of the 4 different substrates.

The wettability of the prepared substrates was assessed by measuring the static water contact angle (WCA) using an optical tensiometer (Attension Theta, Biolin Scientific). The tests were conducted under sequential 10 min UV irradiation while the substrates were submerged under a thin layer of deionised water. After UV exposure, the samples were dried before WCA measurement. For this, 3 μL droplets of deionised water were deposited onto the substrates. The static WCAs were obtained by fitting the drop profile to a Young–Laplace curve.

Accelerated weathering tests were performed following the standard norm: ISO 11507 Method A using a weathering chamber (QUV/basic model, Micom Laboratories Inc.). A cycle with two steps was selected. During the first step, the samples are irradiated with UV light (0.71 W m^{-2}) at 60 °C for 4 hours. The second step consists of water condensation at 50 °C. These steps were repeated consecutively and the samples were taken for analysis at four different times: 100 h, 200 h, 400 h and 600 h.

Evaluation of the artificial weathering effects on the AR films was carried out by SEM imaging, optical transmittance measurements and chemical changes detected by infrared spectroscopy (FT-IR) in attenuated total reflectance mode (Alpha FTIR, Bruker).

The nanomechanical characterization of the AR nanostructured surfaces was performed by nanoindentation and nanoscratch tests using a Hysitron TriboIndenter (TI 950 instrument). A spherical diamond tip with a radius of 10 μm was employed as the indenter probe. Each nanoindentation test consisted of 20 load-controlled load–hold–unload cycles unloading to 50% of the maximum load in each cycle until a maximum total load of 200 μN was reached. A minimum of 10 indentations were performed on each sample. The nanoscratch testing consisted of scratches of 16 μm in length, using a constant normal force of 100 μN. Two additional scans with a low normal force of 2 μN were programmed before and after each scratch in order to obtain the topography profile of the scratched line before and after the test to calculate the residual depth of the scratch.

3. Results and discussion

The production of nanostructured multifunctional AR surface composite films is carried out using a single thermal nanoimprint process. PMMA is employed as a base polymeric material due to its exceptional optical properties, such as low light absorption and transmittance values higher than 90% in the visible spectrum. The fabrication method of the composite nanostructured films is outlined in Fig. 1. Initially, the

required TiO_2 nanoparticles were synthesized following the hydrothermal method described by Grätzel[39] (see Fig. S1 and Table S1† for characterization details). The fabrication starts by layering a PMMA film of 660 nm onto a flexible PET substrate *via* spin coating of a PMMA solution (Fig. S2† shows the profilometer profile). Subsequently, a methanol dispersion of the TiO_2 nanoparticles is spin-coated onto the PMMA film. Three different dispersion concentrations were employed (0.1, 0.5 and 1 wt%) in order to determine the impact of the nanoparticle load on the nanoimprinting pattern fidelity as well as on the final properties of the AR films. The spin coating process of the TiO_2 particles produces a monolayer of particles on the surface of the PMMA substrate with a maximum height of 33 nm (see AFM images in Fig. S3†). In the next step, the films are imprinted in a thermal process using a PDMS working mould patterned with the moth-eye topography. After cooling, the film is de-moulded obtaining the polymer moth-eye structures filled with polymer dispersed nanoparticles. The fabrication process is shown in the scheme of Fig. 1a. Double-sided AR films were also fabricated by imprinting a double-sided coated substrate placed between two PDMS AR moulds. The neat PMMA imprinted film is denoted as P-AR and the imprinted composite films are denoted as P-01T-AR, P-05T-AR, and P-1T-AR in reference to the initial TiO_2 dispersion concentrations employed. The quality of the replication was assessed by SEM and AFM imaging. The height of the cone-like features obtained ranged from 340 nm for the P-AR film to 290 nm for the P-1T-AR nanocomposite film (see AFM profiles in Fig. S4 and S5† and geometrical parameters in Table S2†). This gradual decrease in the cone height is presumably caused by the increase in viscosity of the softened polymer with the particle load impacting the flow of the polymer into the cavities of the mould during the imprinting process. The AFM and SEM images in Fig. 1b and c show a moth-eye topography imprinted on the 0.5 wt% TiO_2 composite (P-05T-AR); Fig. 1d corresponds to a SEM cross-section image of this film. Both images

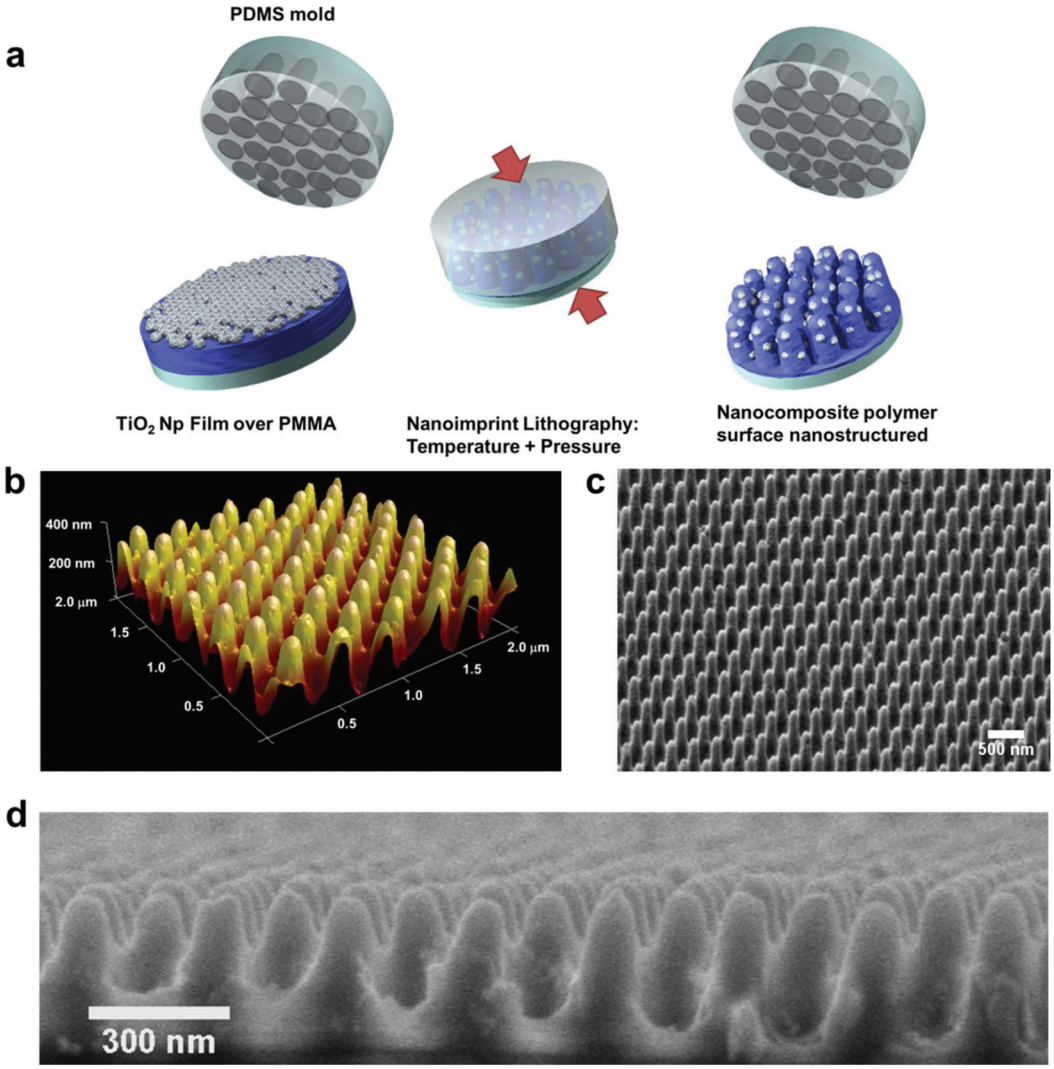

Fig. 1 (a) Scheme of the fabrication process of AR moth-eye nanocones on PMMA–TiO_2 nanocomposites. (b–d) Morphological characterization of a P-05T-AR substrate surface, (b) 3D-AFM topography image, (c) SEM image of a tilted sample, (d) SEM image of the cross-section.

show well-formed cone-like nanostructures with TiO_2 nanoparticles distributed on the imprinted layer of nanocone tips as well as on the valleys.

The optical performance of the nanocomposite moth-eye surfaces was characterized using a spectrophotometer equipped with an optical integrating sphere. This equipment allowed determining the total reflectance at an incidence angle of 8°. The optical performance of the nanocomposites prepared with different loads of TiO_2 imprinted on a single side and on both sides was characterized and compared to a neat polymer flat surface as a reference. The optical characterization results are summarized in Fig. 2. As can be seen, the moth-eye nanostructures reduced significantly the broadband reflectance seen on the flat film from values of about 9% to 6% (Fig. 2b). Due to the high refractive index of titania (~2.5), a reduction in the transmittance and therefore, an increase in the reflected component was seen as the amount of nanoparticles increased on the films. The P-01T-AR film presented similar reflectance values to those of the neat film, while these increased slightly for P-05T-AR and P-1T-AR films signifying the absorption and scattering effects by the TiO_2 particles as the load increased. Nonetheless, these results also reveal that a thin monolayer of nanoparticles such that applied on the surfaces does not deteriorate the optical properties of the AR films significantly and in fact, all the AR composite films showed a strong broadband reflectance reduction over the reference neat PMMA flat film. Remarkably, the total reflectance of P-01T-AR and P-05T-AR films imprinted with moth-eye features on both sides, reached values below 1% for wavelengths in the region of 600 nm, and below 2% in most of the visible part of the spectrum. The specular transmittance measurements are shown in Fig. 2a. In this figure, it can be seen that in accordance with the level of reflection, the transmittance values were above 90% within the range from 400 nm to 700 nm, which is higher than that of the flat film (~88%).

The extended transmission and reflection spectra (200–2000 nm) are shown in Fig. S6.† The substrates being made of two layers of different plastic materials showed the typical UV absorption in the 300–400 nm range. In addition, the higher amount of titania in the P-1T-AR substrate produced a discernible decrease in transmittance below the 425 nm wavelength range, while the transmittance observed through the P-01T-AR substrate was very close to that of the neat P-AR substrate. Likewise, the transmission spectra of the

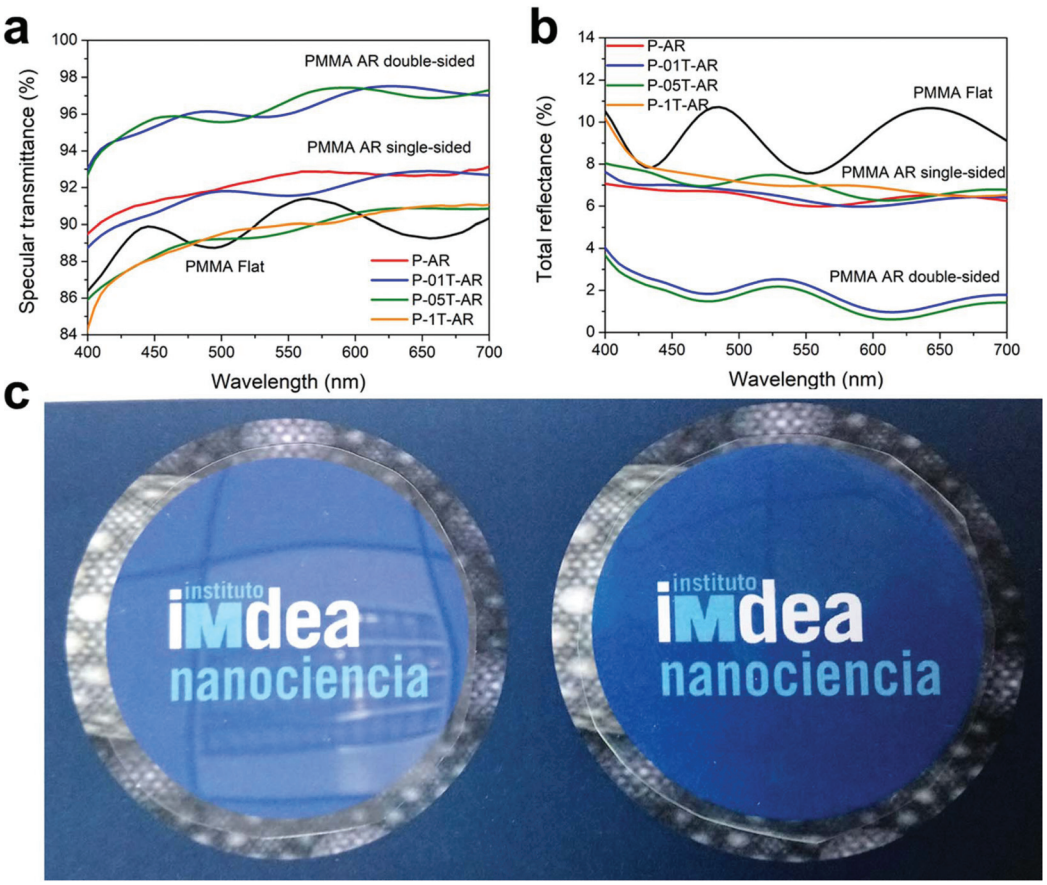

Fig. 2 Characterization of the broadband transmission and anti-reflective properties. (a)Specular transmission spectra. (b) Total reflection spectra. (c) Photographs demonstrating the reflection reduction caused by the moth-eye structures on P-05T-AR film (right) over a PET film and a PMMA coated PET film (left).

substrates P-01T-AR and P-05T-AR imprinted on both sides displayed values as high as 98%, indicating that there were practically no optical losses due to absorption or diffuse scattering effects by the TiO_2 nanoparticles.

A consistent decrease in optical transmittance for all imprinted substrates (with or without titania) in the region from 435 to 400 nm was also noted. To ascertain the origin of this drop, the transmittance of substrates with no TiO_2 particles and with and without structures were comparatively measured (see transmission spectra in Fig. S7†). These measurements proved that the optical scattering losses caused by the moth-eye nanostructures are responsible for the slight drop in transmittance seen in that region. The thin layer of well-dispersed TiO_2 nanoparticles within the polymer matrix in fact did not impair the optical transparency of the moth-eye films and this is illustrated by the digital photograph in Fig. 2c. The photograph shows the high transparency and the reflection reduction brought about by the moth-eye structures on the P-05T-AR printed film (right) compared to a non-patterned PMMA film where the reflected image of the ceiling can be clearly perceived (left).

The photo-induced self-cleaning effect was assessed by monitoring the degradation of the dye Rhodamine B (RhB) with UV radiation. For this, the AR substrates prepared with different TiO_2 loads were exposed to UV radiation at regular intervals of 10 min immersed under a thin layer of water to emulate a humid or wet environment.[40] Fig. 3a shows the relative RhB concentration variation due to photo-catalytic degradation after sequential UV radiation doses. As a control substrate, a neat P-AR film was used (red line). The slight degradation with the exposure time observed for the RhB on this control can be attributed to the photobleaching induced by the UV light on RhB. For the imprinted nanocomposite films, all showed a photocatalytic activity that increased with the TiO_2 load and exposure time. As expected, the maximum degradation was obtained for the P-1T-AR composite. On this substrate, the RhB was degraded approximately 70% after 70 min of UV exposure. In this period of time, P-01T-AR showed 30% degradation only. Tests were carried out to determine the effect of the thermal imprint process on the photocatalytic activity of the TiO_2 loaded on the three different substrates (see Fig. S8† for the plotted results). The substrates with 0.5 and 1% TiO_2 surface load, moth-eye imprinted and non-imprinted or flat, showed a similar catalytic efficiency. However, in the case of 0.1% TiO_2 load, the imprinted AR substrates displayed a marked reduction in photocatalytic efficiency. This result signifies that in the case of the P-01T-AR substrate, with more dispersed nanoparticles, the incorporation of these into the nanocones by the polymer flow during imprinting is more efficient which is in good agreement with the height of the nanocones obtained (see profile in Fig. S5†). In the case of higher loads, (0.5% and 1%), the titania particles form a quasi-continuous film (see AFM images in Fig. S3†) whereby the interaction forces among nanoparticles are stronger which possibly results in a less efficient integration of the nanoparticles into the matrix and as a result, the nanoparticles are less embedded showing similar photocatalytic efficiency to the non-imprinted substrates.

To evaluate the photoinduced surface wettability, the different AR composite films were irradiated with UV light through a thin water layer and after drying, the wettability of the substrates was determined through water contact angle (WCA) measurements at the same regular intervals. Newly imprinted AR surfaces displayed a WCA of about 135°. This angle was the same for both the neat or composite AR surfaces. The consistency found in all the surfaces indicates that the surface roughness of all the substrates was alike with nanoparticles embedded into the polymer topography as confirmed by AFM (Fig. 1b). The WCA on the neat and P-01T-AR surfaces remained hydrophobic with only a slight drop in the WCA value. However, the WCA for the P-05T-AR and P-1T-AR substrates decreased over time after exposure to UV light and at around 40 min of irradiation, the surfaces became hydrophilic as shown in Fig. 3b. The initial hydrophobicity recovered minimally over a period of months (see Fig. S9†) and only after heating at temperatures above 80 °C,

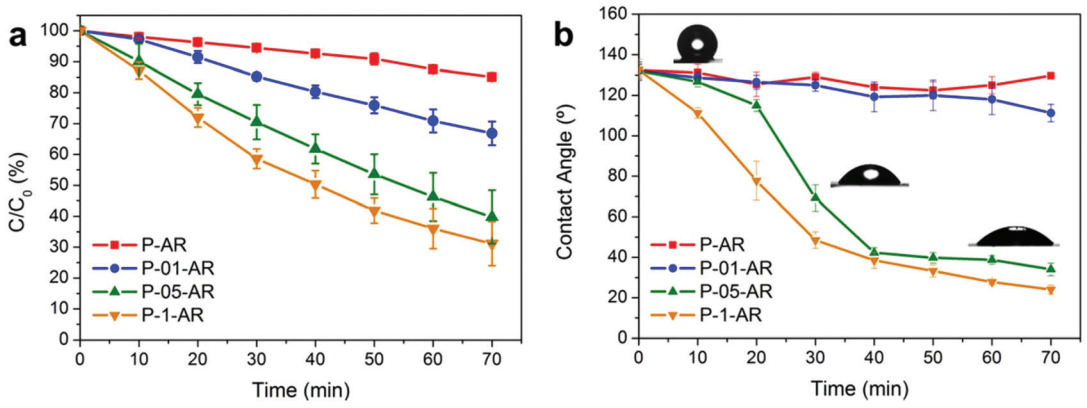

Fig. 3 (a)Photocatalytic activity for different TiO_2 loads on the composite substrates with UV radiation time measured as the decrease in concentration of Rhodamine B by photocatalytic decomposition; (b) wettability conversion on the TiO_2 composite surfaces (hydrophobic–hydrophilic) measured by changes in contact angle as a function of the UV irradiation time under wet conditions.

the initial hydrophobicity was restored. These results concur with the photocatalytic activity observed for the TiO_2 composites where the surfaces with higher TiO_2 load (0.5–1 wt%) sustained a higher degree of photocatalysis. The wettability switch of TiO_2 polymer nanocomposite surfaces has been reported before.[25,41] From X-ray photoelectron spectroscopy (XPS) measurements the switch has been associated with an increase in the content of Ti–OH on the surface upon UV exposure.[25]

An accelerated weathering test was programmed in order to investigate the aging resistance of the different substrates. The test was performed applying UV radiation, temperature and humidity cycles following the standard ISO 11507 utilizing a climate chamber. The morphological changes induced by the accelerated weathering were determined by SEM. The images indicate that the P-01T-AR nanostructures remained unchanged even after 600 h. However, for the P-05T-AR and P-1T-AR films an appreciable increase in roughness and exposure of nanoparticles on the surfaces could be seen with increasing radiation time signifying the loss of the polymer matrix due to photocatalytic degradation (see Fig. S10† for SEM images of the surfaces after weathering). These results underline the need for an optimal content of TiO_2 nanoparticles to achieve the desired photocatalytic effect with minimal polymer degradation. The optical quality of the AR film tested was studied after each weathering cycle by measuring the specular transmittance (see Fig. S11†). The substrates show a decrease in transmittance when the ageing time and amount of titania nanoparticles increased. The resistance to wear of the P-01T-AR films with 0.1 wt% of titania nanoparticles is worth remarking, showing values of 88% transmittance after 600 h of weathering. The chemical changes taking place after the aging process were also evaluated by attenuated total reflection Fourier transform infrared spectroscopy (FTIR-ATR) (Fig. S12† summarizes the FTIR-ATR spectra obtained). The P-AR and P-01T-AR did not show any appreciable chemical change after 600 h of weathering cycles. However, after 200 h of weathering, the P-05T-AR and P-1T-AR substrates showed a marked reduction of the PMMA IR bands indicating a significant degradation of the PMMA matrix due to photooxidation reactions. The absence of new peaks corresponding to degraded compounds after weathering suggests that chain scission and de-polymerization are the most prevalent degradation mechanisms of PMMA.[42]

The mechanical robustness of the AR nanocomposite surfaces was characterized by nanoindentation. Nanoindentation has demonstrated to be a valuable technique for the mechanical characterization of polymer nanocomposites and because of its high sensitivity to small surface deformations, has also become a useful tool for the measurement of mechanical properties of surface nanostructures.[43,44] Here, nanoindentation and nanoscratch experiments were specifically designed for studying the deformation resistance of the imprinted AR nanostructures to normal and lateral stresses, respectively. Nanoindentation tests were performed applying incremental load–unload cycles onto the sample surface using a nanoindenter equipped with a 10 μm radius spherical tip until a final load of 200 μN was applied. This load was preselected from load–displacement curves where the penetration depths attained were smaller than the height of the moth-eye nanocone structures. Representative load–depth curves obtained for each of the tested samples are plotted in Fig. 4a. The flat substrate presented initially an elastic response for which the loading and unloading segments in each loading cycle overlapped, while the imprinted samples presented less elastic recovery with more permanent deformation at lower loads. The maximum indentation depth at 200 μN was substantially lower

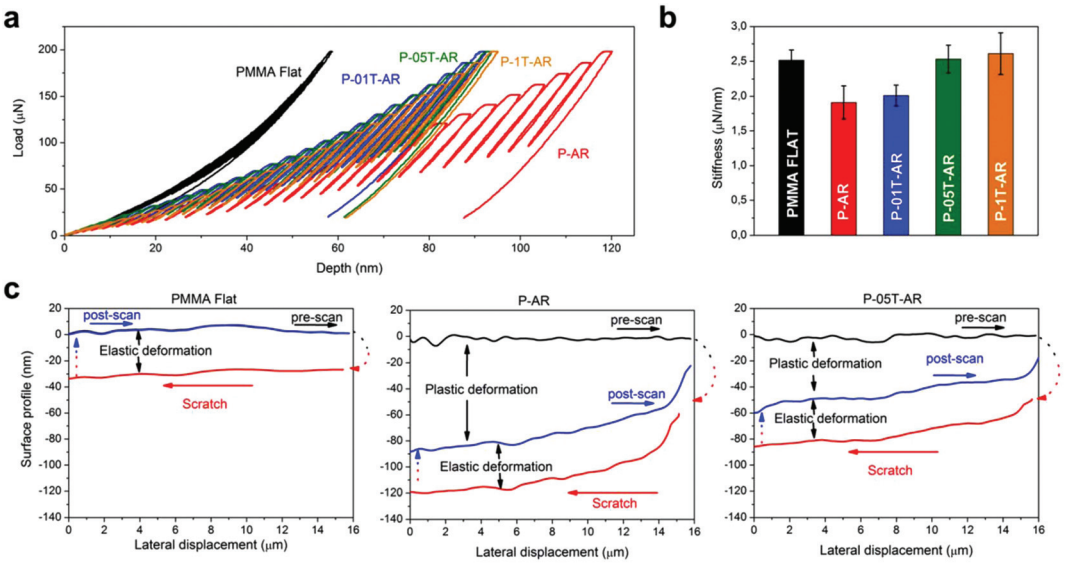

Fig. 4 Mechanical properties of the nanocomposite surfaces measured by nanoindentation: (a) indentation load–depth curves, (b) stiffness values obtained in the elastic region, (c) scratch test results for three representative samples: PMMA flat, P-AR and P-05T-AR.

for the flat sample (≈50 nm), than for the P-AR sample (≈120 nm). The addition of TiO_2 nanoparticles improved considerably the mechanical resistance of the moth-eye imprinted surfaces due to their higher elastic modulus with a reduction in maximum depth up to ≈90 nm. It is worth noting that in all experiments the maximum indenter depth reached was lower than the height of nanostructures that ranged from 290 to 340 nm and therefore, the experiments essentially are indicative of the mechanical behaviour of the nanostructures. Interestingly, the moth-eye imprinted surfaces with three different TiO_2 loads (P-01T-AR, P-05T-AR, P-1T-AR) did not show apparent differences in the mechanical strength (Fig. 4a), suggesting that the quantity of nanoparticles that is incorporated inside the nanostructures is comparable regardless of the initial concentration applied onto the surface. The contact stiffness did however change with the load of TiO_2 nanoparticles. Fig. 4b plots the contact stiffness obtained from the initial slope of the indentation load–depth curve in the elastic region, at a penetration of ≈10 nm where plastic deformation is negligible. The stiffness decreased from 2.5 to 1.9 μN nm^{-1} upon imprinting the moth-eye nanostructures on the neat PMMA film. This is presumably due to the decrease in the effective area in contact upon imprinting the surface. However, the stiffness increased successively with the TiO_2 particle loading and reached up to ≈2.6 μN nm^{-1} in the P-1T-AR substrate. This corresponds to a stiffness enhancement of 37% over the neat P-AR substrate and a value similar to that of the flat PMMA surface. Considering that the geometrical parameters of the nanostructures were equivalent for all the imprinted AR composites, this result indicates that increasing nanoparticle concentration does increase the stiffness owing to the higher nanoparticle loading remaining at the base of the AR nanocones rather than on the cones themselves, which as seen above, appears equivalent. Thus, this result confirms the good integration of the TiO_2 nanoparticles on the matrix and its reinforcement effect.[34]

Nanoscratches with a length of 16 μm were performed at a constant normal force of 100 μN to evaluate the scratch resistance (see the load profile in Fig. S13†). The results are presented in Fig. 4c. The normal force during scratching was selected to maintain a maximum penetration below the height of the moth-eye nanostructures. Initially a pre-scan was performed whereby the length of the scratch was first scanned with a small contact force (2 μN) to acquire the topographical height profile. Subsequently, the scratch was produced and afterwards, a post-scan was performed at low contact force to evaluate the residual scratch depth. The arrows on the plots indicate the direction of the scans during the experiment (left-to-right for the pre- and post-scans, right-to-left for the scratch experiment). The differences between the height profiles of the pre- and post-scans indicate the permanent residual deformation left by the scratch, while the difference between the height profiles obtained during scratching and the post-scan corresponds to the elastic recovery. As can be seen in Fig. 4c, the flat PMMA surface undergoes a scratch depth of ≈35 nm but it does not suffer any permanent deformation under the selected working force because the pre and post-scans overlap completely (black and blue lines). Imprinting moth-eye features on the neat PMMA (P-AR graph) results in a substantially reduced scratch resistance, with a total scratch depth of ≈120 nm, of which, only ≈30 nm are elastically recovered leaving a residual scratch depth of ≈90 nm. However, loading the imprinted surfaces with TiO_2 nanoparticles resulted in a substantially enhanced scratch resistance with a residual scratch depth below 60 nm for the P-05T-AR substrate. Comparable results were obtained for P-01T-AR and P-1T-AR substrates (see Fig. S14†). Consistent with the results obtained through the nanoindentation experiments, the scratch tests support the presumption that the incorporation of the nanoparticles inside the nanostructures is size constrained by the nanocone volume. SEM images of the scratch regions in Fig. S15† show a scratch damage limited to the tip of the nanocones corroborating the nanoscratch measurements.

4. Conclusions

This paper has presented a practical methodology to produce broadband anti-reflective and photo-induced cleaning polymer composite surfaces with improved durability and mechanical resistance. These multifunctional films have been produced on titania polymer nanocomposite surfaces *via* nanoimprinting of an antireflective moth-eye inspired topography. The films presented excellent optical performance being anti-reflective and highly transparent while containing a thin titania load. Additionally all the nanocomposite films presented a self-cleaning function derived from photocatalytic activity and photo-induced hydrophilicity activated by UV light. The accelerated weathering tests indicated that with 0.1% TiO_2 loading, the film matrix does not experience an apparent photo-degradation after 600 h, maintaining higher optical quality. Conversely, a larger amount of nanoparticles induced the degradation of the PMMA nanostructure matrix, deteriorating the optical properties after 100 h of accelerated weathering. Hence, considerations have to be made on the loading quantity of titania nanoparticles based on the specific application and the desired lifetime. Alternatively, a polymer matrix more stable towards photo-degradation such as fluorinated polymers can be used. Nanomechanical tests provided evidence for an enhanced mechanical robustness of the nanocomposite AR surfaces to both normal and lateral loadings with respect to neat AR surfaces. It is perfectly plausible to adapt the fabrication of the multifunctional AR-TiO_2 composites to coating–imprinting sequential roll-to-roll processing methodology for large scale and low cost production. Moreover, the approach presented can be adopted for other polymer/nano-reinforced systems with added functionalities.

Conflicts of interest

The authors declare the following competing financial interest: the authors have applied for a patent on the topic of this paper.

Acknowledgements

The present work was performed within the framework of the NANOLEAP project. This project has received funding from the European Union's Horizon 2020 Research and Innovation Program under the grant agreement no 646397. The research has been partially supported by the Ministry of Education and Research of the Madrid Community (ref. PEJ15/IND/AI-0626) and the European Social Fund (ESF). The authors are grateful to the personnel of the Institute of Optica "Daza de Valdés", IO-CSIC, Madrid, for the equipment support on the optical characterization and to Irene Sevilla de la Llave y Javier Sacristán Bermejo from ACCIONA Construction Technological Center for performing the accelerated weathering tests and for the technical assistance designing the experiments. IMDEA Nanociencia acknowledges support from the Severo Ochoa Programme for Centres of Excellence in R&D (MINECO, Grant SEV-2016-0686).

References

1 L. Yao and J. He, *Prog. Mater. Sci.*, 2014, **61**, 94–143.
2 H. K. Raut, V. A. Ganesh, A. S. Nair and S. Ramakrishna, *Energy Environ. Sci.*, 2011, **4**, 3779–3804.
3 P. Vukusic and J. R. Sambles, *Nature*, 2003, **424**, 852–855.
4 W.-K. Kuo, J.-J. Hsu, C.-K. Nien and H. H. Yu, *ACS Appl. Mater. Interfaces*, 2016, **8**, 32021–32030.
5 Z. Diao, M. Kraus, R. Brunner, J. H. Dirks and J. P. Spatz, *Nano Lett.*, 2016, **16**, 6610–6616.
6 Z. Diao, J. Hirte, W. Chen and J. P. Spatz, *ACS Omega*, 2017, **2**, 5012–5018.
7 W.-L. Min, B. Jiang and P. Jiang, *Adv. Mater.*, 2008, **20**, 3914–3918.
8 J. Zhang, S. Shen, X. X. Dong and L. S. Chen, *Opt. Express*, 2014, **22**, 1842–1851.
9 B. Ai, P. Gu, H. Mohwald and G. Zhang, *Nanoscale*, 2016, **8**, 15473–15478.
10 H. K. Raut, S. S. Dinachali, Y. C. Loke, R. Ganesan, K. K. Ansah-Antwi, A. Góra, E. H. Khoo, V. A. Ganesh, M. S. M. Saifullah and S. Ramakrishna, *ACS Nano*, 2015, **9**, 1305–1314.
11 W. Chen, Z. Diao, J. H. Dirks, F. Geiger and J. Spatz, *Macromol. Mater. Eng.*, 2017, **302**, 1700072.
12 G. Tan, J.-H. Lee, Y.-H. Lan, M.-K. Wei, L.-H. Peng, I. C. Cheng and S.-T. Wu, *Optica*, 2017, **4**, 678–683.
13 J. Li, J. Zhu and X. Gao, *Small*, 2014, **10**, 2578–2582.
14 J. van de Groep, P. Spinelli and A. Polman, *Nano Lett.*, 2015, **15**, 4223–4228.
15 M. Burghoorn, D. Roosen-Melsen, J. de Riet, S. Sabik, Z. Vroon, I. Yakimets and P. Buskens, *Materials*, 2013, **6**, 3710.
16 J. Cai and L. Qi, *Mater. Horiz.*, 2015, **2**, 37–53.
17 X. Li, X. Yu and Y. Han, *J. Mater. Chem. C*, 2013, **1**, 2266–2285.
18 M. E. Calvo, J. R. Castro Smirnov and H. Míguez, *J. Polym. Sci., Part B: Polym. Phys.*, 2012, **50**, 945–956.
19 N. Abidi, L. Cabrales and E. Hequet, *ACS Appl. Mater. Interfaces*, 2009, **1**, 2141–2146.
20 A. M. Ramirez, K. Demeestere, N. De Belie, T. Mäntylä and E. Levänen, *Build. Sci.*, 2010, **45**, 832–838.
21 R. Núñez-Lozano, B. Pimentel, J. R. Castro-Smirnov, M. E. Calvo, H. Míguez and G. de la Cueva-Méndez, *Adv. Healthcare Mater.*, 2015, **4**, 1944–1948.
22 D. Scalarone, M. Lazzari and O. Chiantore, *Polym. Degrad. Stab.*, 2012, **97**, 2136–2142.
23 I. Hincapié, T. Künniger, R. Hischier, D. Cervellati, B. Nowack and C. Som, *J. Nanopart. Res.*, 2015, **17**, 287.
24 J. Zhang and Y. Nosaka, *J. Phys. Chem. C*, 2014, **118**, 10824–10832.
25 Q. F. Xu, Y. Liu, F.-J. Lin, B. Mondal and A. M. Lyons, *ACS Appl. Mater. Interfaces*, 2013, **5**, 8915–8924.
26 S. Singh, H. Mahalingam and P. K. Singh, *Appl. Catal., A*, 2013, **462–463**, 178–195.
27 F. Petronella, A. Truppi, C. Ingrosso, T. Placido, M. Striccoli, M. L. Curri, A. Agostiano and R. Comparelli, *Catal. Today*, 2017, **281**(Part 1), 85–100.
28 V. Binas, D. Venieri, D. Kotzias and G. Kiriakidis, *J. Materiomics*, 2017, **3**, 3–16.
29 R. Fateh, R. Dillert and D. Bahnemann, *Langmuir*, 2013, **29**, 3730–3739.
30 C. R. Crick, J. C. Bear, A. Kafizas and I. P. Parkin, *Adv. Mater.*, 2012, **24**, 3505–3508.
31 E. Ukaji, T. Furusawa, M. Sato and N. Suzuki, *Appl. Surf. Sci.*, 2007, **254**, 563–569.
32 F. Xu, T. Wang, H. Chen, J. Bohling, A. M. Maurice, L. Wu and S. Zhou, *Prog. Org. Coat.*, 2017, **113**, 15–24.
33 T. V. Nguyen, P. Nguyen Tri, T. D. Nguyen, R. El Aidani, V. T. Trinh and C. Decker, *Polym. Degrad. Stab.*, 2016, **128**, 65–76.
34 S. Guldin, P. Kohn, M. Stefik, J. Song, G. Divitini, F. Ecarla, C. Ducati, U. Wiesner and U. Steiner, *Nano Lett.*, 2013, **13**, 5329–5335.
35 K. Nakata, M. Sakai, T. Ochiai, T. Murakami, K. Takagi and A. Fujishima, *Langmuir*, 2011, **27**, 3275–3278.
36 S. M. Kang, S. Jang, J.-K. Lee, J. Yoon, D.-E. Yoo, J.-W. Lee, M. Choi and N.-G. Park, *Small*, 2016, **12**, 2443–2449.
37 S. Jang, S. M. Kang and M. Choi, *ACS Appl. Mater. Interfaces*, 2017, **9**, 44038–44044.
38 A. M. Díez-Pascual, M. A. Gómez-Fatou, F. Ania and A. Flores, *Prog. Mater. Sci.*, 2015, **67**, 1–94.
39 S. D. Burnside, V. Shklover, C. Barbé, P. Comte, F. Arendse, K. Brooks and M. Grätzel, *Chem. Mater.*, 1998, **10**, 2419–2425.
40 H. B. Wu, H. H. Hng and X. W. Lou, *Adv. Mater.*, 2012, **24**, 2567–2571.
41 Y. Qing, C. Yang, N. Yu, Y. Shang, Y. Sun, L. Wang and C. Liu, *Chem. Eng. J.*, 2016, **290**, 37–44.
42 N. Daraboina and G. Madras, *Ind. Eng. Chem. Res.*, 2008, **47**, 6828–6834.
43 J. J. Hernández, M. A. Monclús, I. Navarro-Baena, F. Viela, J. M. Molina-Aldareguia and I. Rodríguez, *Sci. Rep.*, 2017, **7**, 43450.
44 A. Skarmoutsou, C. A. Charitidis, A. K. Gnanappa, A. Tserepi and E. Gogolides, *Nanotechnology*, 2012, **23**, 505711.

